

# Implicit-explicit Runge-Kutta methods for the two-fluid MHD equations

H. Kumar

Research Report No. 2011-26  
May 2011

Seminar für Angewandte Mathematik  
Eidgenössische Technische Hochschule  
CH-8092 Zürich  
Switzerland

# Implicit-Explicit Runge-Kutta Methods for the Two-fluid MHD Equations

Harish Kumar<sup>1a</sup>

<sup>a</sup>*Seminar for Applied Mathematics, D-MATH,  
ETH Zurich, CH-8092*

---

## Abstract

Two-fluid ideal magnetohydrodynamics (MHD) equations are a generalized form of the ideal MHD equations in which the electrons and ions are considered as separate species. A major difficulty in the design of efficient numerical algorithms for these equations is the presence of stiff source terms, particularly for realistic charge to mass ratio (i.e. low Larmor radius). Following [9, 10, 11], we design implicit-explicit (IMEX) Runge-Kutta (RK) time stepping schemes. The numerical flux is treated explicitly with strong stability preserving (SSP)-RK methods and the stiff source term is treated implicitly using implicit Runge-Kutta methods. The special structure of the two-fluid MHD equations enable us to split the source terms carefully and ensure that only local (in each cell) equations need to be solved at each time step. Benchmark numerical experiments are presented to illustrate the efficiency of this approach.

*Keywords:* Implicit Explicit Runge-Kutta Method, Two-fluid MHD, Plasma flows, Hyperbolic systems

---

## 1. Introduction

Flows in plasmas are frequently modeled by the equations of ideal magnetohydrodynamics (MHD). These equations combine the Euler equations for compressible flow together with Maxwell equations for magnetic fields. These equations assume *quasi-neutrality* of the plasma i.e. the difference in number density of ions and electrons is ignored.

However, in many applications like fast magnetic reconnection, the assumption of quasi-neutrality is violated. In such cases, one resorts to extended MHD models. A popular example consider the flow of two different species, one electron and one ion, species separately. This results in the so-called two fluid MHD equations (see [1], [2]). In non-dimensional conservative variables these equations are:

$$\frac{\partial \rho_i}{\partial t} + \nabla \cdot (\rho_i \mathbf{v}_i) = 0, \quad (1.1a)$$

$$\frac{\partial(\rho_i \mathbf{v}_i)}{\partial t} + \nabla \cdot (\rho_i \mathbf{v}_i \mathbf{v}_i^\top + p_i \mathbf{I}) = \frac{1}{\hat{r}_g} \rho_i (\mathbf{E} + \mathbf{v}_i \times \mathbf{B}), \quad (1.1b)$$

$$\frac{\partial \mathcal{E}_i}{\partial t} + \nabla \cdot ((\mathcal{E}_i + p_i) \mathbf{v}_i) = \frac{1}{\hat{r}_g} \rho_i (\mathbf{E} \cdot \mathbf{v}_i), \quad (1.1c)$$

$$\frac{\partial \rho_e}{\partial t} + \nabla \cdot (\rho_e \mathbf{v}_e) = 0, \quad (1.1d)$$

$$\frac{\partial(\rho_e \mathbf{v}_e)}{\partial t} + \nabla \cdot (\rho_e \mathbf{v}_e \mathbf{v}_e^\top + p_e \mathbf{I}) = -\frac{\lambda_m}{\hat{r}_g} \rho_e (\mathbf{E} + \mathbf{v}_e \times \mathbf{B}), \quad (1.1e)$$

$$\frac{\partial \mathcal{E}_e}{\partial t} + \nabla \cdot ((\mathcal{E}_e + p_e) \mathbf{v}_e) = -\frac{\lambda_m}{\hat{r}_g} \rho_e (\mathbf{E} \cdot \mathbf{v}_e), \quad (1.1f)$$

$$\frac{\partial \mathbf{B}}{\partial t} + \nabla \times \mathbf{E} + \kappa \nabla \psi = 0, \quad (1.1g)$$

---

<sup>1</sup>harish@math.ethz.ch

$$\frac{\partial \mathbf{E}}{\partial t} - \hat{c}^2 \nabla \times \mathbf{B} + \xi \hat{c}^2 \nabla \phi = -\frac{1}{\hat{\lambda}_d^2 \hat{r}_g} (r_i \rho_i \mathbf{v}_i + r_e \rho_e \mathbf{v}_e), \quad (1.1h)$$

$$\frac{\partial \phi}{\partial t} + \xi \nabla \cdot \mathbf{E} = \frac{\xi}{\hat{\lambda}_d^2 \hat{r}_g} (r_i \rho_i + r_e \rho_e), \quad (1.1i)$$

$$\frac{\partial \psi}{\partial t} + \kappa \hat{c}^2 \nabla \cdot \mathbf{B} = 0. \quad (1.1j)$$

Here, the subscript  $\{i, e\}$  refers to the ion and electron species respectively,  $\rho_{\{i, e\}}$  are densities,  $\mathbf{v}_{\{i, e\}} = (v_{\{i, e\}}^x, v_{\{i, e\}}^y, v_{\{i, e\}}^z)$  are velocities,  $\mathcal{E}_{\{i, e\}}$  are the energies,  $p_{\{i, e\}}$  are the pressures,  $\mathbf{B} = (B^x, B^y, B^z)$  is the magnetic field,  $\mathbf{E} = (E^x, E^y, E^z)$  is the electric field,  $\phi, \psi$  are the potentials and  $\xi, \kappa$  are the speeds for Maxwell equations. Also,  $r_\alpha = q_\alpha/m_\alpha$ ,  $\alpha \in \{i, e\}$  are the charge-mass ratios and  $\lambda_m = m_i/m_e$  is the ion-electron mass ratio.

Several physically significant parameters appear in the non-dimensionalized form (1.1) of the two-fluid equations. Here,  $\hat{r}_g = \frac{r_g}{x_0} = \frac{m_i v_i^T}{q_i B_0 x_0}$  is the normalized ion Larmor radius,  $\hat{c} = c/v_i^T$  is the normalized speed of light and  $\hat{\lambda}_d = \lambda_d/r_g = \sqrt{\varepsilon_0 v_i^{T2}/n_0 q_i}/r_g$  is the ion Debye length normalized with Larmor radius. Also,  $v_i^T$  is the reference thermal velocity of ions,  $B_0$  is the reference magnetic field and  $x_0$  is the reference length. Ion mass  $m_i$  is assumed to be 1. In addition, we assume that both the ion and the electron species satisfies the ideal gas law:

$$\mathcal{E}_\alpha = \frac{p_\alpha}{\gamma - 1} + \frac{1}{2} \rho_\alpha |\mathbf{v}_\alpha|^2, \quad \alpha \in \{i, e\}. \quad (1.2)$$

with  $\gamma = 5/3$ . Eqns. (1.1a)-(1.1c) represent the conservation of mass, momentum and energy for the ions. The source term in (1.1b) represents the Lorentz force acting on ions due to the electric and magnetic fields. Similarly Eqns.(1.1d)-(1.1f) represent conservation of these quantities for electrons. Eqns. (1.1g)-(1.1j) are the perfectly hyperbolic Maxwell's (PHM) equations (see [3]). These equations satisfy the divergence constraint approximately and are consistent with the hyperbolic structure of the fluid equations. Note that when the Larmor radius  $\hat{r}_g \rightarrow 0$ , the two-fluid model approaches the MHD limit. Similarly for  $\hat{r}_g \rightarrow \infty$ , (1.1) reduces to Euler equations for ions and electrons.

The system of two-fluid Eqns. (1.1) is a system of balance laws, and can be written in the form,

$$\mathbf{u}_t + \nabla \cdot \mathbf{f}(\mathbf{u}) = \mathbf{s}(\mathbf{u}). \quad (1.3)$$

Here, the vector of unknowns  $\mathbf{u}$ , the flux vector  $\mathbf{f} = \{\mathbf{f}^x, \mathbf{f}^y, \mathbf{f}^z\}$ , and the source vector  $\mathbf{s}$  can be read from (1.1). It is well known that solutions of (1.3) consist of discontinuities in the form of shocks and contact discontinuities. Numerical algorithms have to take into account the formation of these complex waves and their interactions. Furthermore, in the case of two-fluid equations, source terms can be stiff, especially for realistic physical parameters. Thus, explicit time stepping will be extremely expensive computationally due to small time steps.

Numerical methods for the two-fluid equations have received some attention in recent years. In [2], the authors uses a Roe-type Riemann solver. Time updates are performed by treating the stiff source term implicitly and convection flux terms explicitly. The resulting equations are solved using Newton iterations. This method might be diffusive and may require many iterations for each time step. In [1], the authors propose a wave propagation method (see [4]) for the spatial discretization. For time update a second order operator splitting approach is used. This approach is easy to implement but can be computationally expensive, especially for the stiff source term. In [5, 6] authors, uses a Riemann-solver-free central difference scheme for staggered grid based on [7]. However, numerical simulations uses artificial physical parameters, to avoid stiffness in the source.

In this article, we present implicit-explicit (IMEX) Runge-Kutta (RK) schemes for the two-fluid Eqns. (1.1) based on explicit treatment of convective flux using strong stability preserving (SSP) schemes (see [8]) and implicit treatment of the stiff source term (see [9, 10]). The resulting system of linear equations (in each cell) are solved exactly.

Rest of the paper is organized as follows: In Section 2, we describe second order spatial discretization of the two-fluid equations (1.1) based on Finite Volume Methods (FVM). In Section 3, we describe explicit

SSP-RK time stepping methods. In Section 4, we present several IMEX-RK time stepping routines for the two-fluid equations. In Section 5, we investigate the performance of these schemes using several numerical test examples.

## 2. Finite Volume Methods

For notational simplicity, we focus on the Eqns. (1.1) in two space dimensions. The extension to three space dimensions is straight forward. We approximate (1.1) in a domain  $(x, y) \in (x_a, x_b) \times (y_a, y_b)$ , discretized uniformly (for simplicity), with mesh size  $\Delta x, \Delta y$  into cells  $I_{ij} = [x_{i-\frac{1}{2}}, x_{i+\frac{1}{2}}] \times [y_{j-\frac{1}{2}}, y_{j+\frac{1}{2}}]$ , where  $x_{i+\frac{1}{2}} = x_i + \Delta x/2$ ,  $y_{j+\frac{1}{2}} = y_j + \Delta y/2$  and  $x_i = x_a + j\Delta x$ ,  $y_j = y_a + j\Delta y$  for the indices  $0 \leq i \leq N_x$ ,  $0 \leq j \leq N_y$ . A semi-crete FVM scheme can be written as,

$$\frac{d\mathbf{U}_{i,j}^n}{dt} = -\frac{1}{\Delta x} \left( \mathbf{F}_{i+\frac{1}{2},j}^{x,n} - \mathbf{F}_{i-\frac{1}{2},j}^{x,n} \right) - \frac{1}{\Delta y} \left( \mathbf{F}_{i,j+\frac{1}{2}}^{y,n} - \mathbf{F}_{i,j-\frac{1}{2}}^{y,n} \right) + \mathbf{s}(\mathbf{U}_{i,j}^n), \quad (2.1)$$

where  $\mathbf{U}_{i,j}^n \approx \frac{1}{\Delta x \Delta y} \int_{I_{i,j}} \mathbf{u}(x, t^n) dx dy$  is the cell average of  $\mathbf{u}$  in the cell  $I_{ij}$  at time level  $t^n$  and  $\mathbf{F}^x$  and  $\mathbf{F}^y$  are numerical fluxes consistent with  $\mathbf{f}^x$  and  $\mathbf{f}^y$  respectively. Note that the flux  $\mathbf{f}$  of two-fluid equations can be divided in to three parts, two nonlinear Euler fluxes (one each for ion and electron) and one linear Maxwell flux for the electromagnetic quantities. The coupling between fluid flow and electromagnetic variables is through the source term only. This allows us to easily construct numerical fluxes. For simplicity, we will describe the numerical flux in the  $x$ -direction i.e.  $\mathbf{F}^x$  only. The expression for the numerical flux in the  $y$ -direction i.e.  $\mathbf{F}^y$ , can be derived similarly.

### 2.1. A four wave HLL type numerical flux

In this article, we will use a four-wave HLL type (see [4]) numerical flux which is described below: Denote  $\mathbf{u} = \{\mathbf{u}_f, \mathbf{u}_m\}^\top$  and  $\mathbf{f}^x(\mathbf{u}) = \{\mathbf{f}_f^x(\mathbf{u}_f), \mathbf{f}_m^x(\mathbf{u}_m)\}^\top$ , with,

$$\mathbf{u}_f = \{\rho_i, \rho_i \mathbf{v}_i, \mathcal{E}_i, \rho_e, \rho_e \mathbf{v}_e, \mathcal{E}_e\}^\top \quad (2.2a)$$

$$\mathbf{f}_f^x = \{\rho_i v_i^x, \rho_i v_i^{x2} + p_i, \rho_i v_i^x v_i^y, \rho_i v_i^x v_i^z, (\mathcal{E}_i + p_i) v_i^x, \rho_e v_e^x, \rho_e v_e^{x2} + p_e, \rho_e v_e^x v_e^y, \rho_e v_e^x v_e^z, (\mathcal{E}_e + p_e) v_e^x\}^\top \quad (2.2b)$$

$$\mathbf{u}_m = \{\mathbf{B}, \mathbf{E}, \phi, \psi\}^\top \quad (2.2c)$$

$$\mathbf{f}_m^x = \{\kappa \psi, -E^y, E^x, \xi \hat{c}^2 \phi, \hat{c}^2 B^y, -\hat{c}^2 B^x, \xi E^x, \kappa \hat{c}^2 B^x\}^\top. \quad (2.2d)$$

We exploit the split structure of the flux in (1.1) and consider the fluid speeds,

$$b_f^l = \min_k \min_\alpha (\lambda_k^\alpha(\mathbf{U}_{f,i,j}^n), \lambda_k^\alpha(\mathbf{U}_{f,a}^n), 0), \quad (2.3a)$$

$$b_f^r = \max_k \max_\alpha (\lambda_k^\alpha(\mathbf{U}_{f,i+1,j}^n), \lambda_k^\alpha(\mathbf{U}_{f,a}^n), 0). \quad (2.3b)$$

Here  $\lambda_k^\alpha \in \{v_\alpha^x - c_\alpha, v_\alpha^x, v_\alpha^x + c_\alpha\}$ ,  $\alpha \in \{i, e\}$  are the eigenvalues of the fluid part, with sound speeds  $c_\alpha = \sqrt{\gamma p_\alpha / \rho_\alpha}$ . Here,  $\mathbf{U}_{f,a}^n$  represent the arithmetics average of states  $\mathbf{U}_{f,i,j}^n$  and  $\mathbf{U}_{f,i+1,j}^n$ . Similarly, let  $b_m^l$  and  $b_m^r$  be the Maxwell HLL speeds, then a four wave HLL type numerical flux for (1.1) can be written as,

$$\mathbf{F}_{i+1/2,j}^{x,n} = \left\{ \mathbf{F}_{f,i+1/2,j}^{x,n}, \mathbf{F}_{m,i+1/2,j}^{x,n} \right\}^\top, \quad (2.4)$$

where

$$\mathbf{F}_{\beta,i+\frac{1}{2},j}^{x,n} = \frac{b_\beta^r \mathbf{f}_\beta^x(\mathbf{U}_{\beta,i,j}^n) - b_\beta^l \mathbf{f}_\beta^x(\mathbf{U}_{\beta,i+1,j}^n)}{b_\beta^r - b_\beta^l} + \frac{b_\beta^r b_\beta^l}{b_\beta^r - b_\beta^l} (\mathbf{U}_{\beta,i+1,j}^n - \mathbf{U}_{\beta,i,j}^n), \quad \beta \in \{f, m\}. \quad (2.5)$$

## 2.2. Second order spatial discretization

The semi-discrete scheme (2.1) with numerical flux (2.4) is only first order accurate. To obtain second order spatial discretization, it is standard to replace the piecewise constant approximation  $\mathbf{U}_{i,j}^n$ , of conservative variables with a piecewise linear reconstruction. As before, we will describe the reconstruction procedure in  $x$ -direction only. The reconstruction in  $y$ -direction is similar.

We suppress the  $j$ -dependence below for notational convenience. Given cell averages  $\mathbf{U}_i^n$ , the reconstruction procedure is carried out component-wise. Let  $U$  be a component of  $\mathbf{U}$ , reconstructed with piecewise linear reconstruction  $p_i^n(x)$  with slope  $\sigma_i^n$  in each cell, then

$$p_i^n(x) = U_i^n + \sigma_i^n(x - x_i).$$

Let us define traces,

$$U_i^{n,+} = p_i^n(x_{i+1/2}), \quad \text{and} \quad U_i^{n,-} = p_i^n(x_{i-1/2}).$$

Then a second order scheme is obtained by replace numerical flux  $\mathbf{F}_{i+1/2}^{x,n} = \mathbf{F}^x(\mathbf{U}_i^n, \mathbf{U}_{i+1}^n)$  in (2.1) with

$$\tilde{\mathbf{F}}_{i+1/2}^{x,n} = \tilde{\mathbf{F}}^x(\mathbf{U}_i^n, \mathbf{U}_{i+1}^n) = \mathbf{F}^x(\mathbf{U}_i^{n,+}, \mathbf{U}_{i+1}^{n,-}). \quad (2.6)$$

In this work, we will use the slope  $\sigma_i^n$ ,

$$\sigma_i^n = \text{minmod} \left( \frac{U_{i+1}^n - U_i^n}{\Delta x}, \frac{U_i^n - U_{i-1}^n}{\Delta x} \right),$$

which corresponds to the MinMod limiter (see [4]). Here,

$$\text{minmod}(a, b) = \begin{cases} \text{sign}(a) \min(|a|, |b|), & \text{if } \text{sign}(a) = \text{sign}(b), \\ 0, & \text{otherwise.} \end{cases}$$

## 3. Explicit time stepping

In this section we will present second- and third-order accurate explicit RK time-stepping scheme for the semi-discrete equation (2.1). These methods are strong stability preserving (SSP) (see [8]).

Let  $\mathbf{U}_{i,j}^n$  is the discrete solution at  $t^n$ , and  $\Delta t = t^{n+1} - t^n$ . Then the semi-discrete scheme (2.1), can be written as,

$$\frac{d\mathbf{U}_{i,j}^n}{dt} = \mathcal{L}_{i,j}(\mathbf{U}^n) + \mathbf{S}_{i,j}(\mathbf{U}^n), \quad (3.1)$$

with,

$$\mathcal{L}_{i,j}(\mathbf{U}^n) = -\frac{1}{\Delta x} \left( \mathbf{F}_{i+1/2,j}^{x,n} - \mathbf{F}_{i-1/2,j}^{x,n} \right) - \frac{1}{\Delta y} \left( \mathbf{F}_{i,j+1/2}^{y,n} - \mathbf{F}_{i,j-1/2}^{y,n} \right), \quad \text{and} \quad \mathbf{S}_{i,j}(\mathbf{U}^n) = \mathbf{s}(\mathbf{U}_{i,j}^n).$$

In order to advance a numerical solution from time  $t^n$  to  $t^{n+1}$ , the SSP-RK algorithm is as follows:

1. Set  $\mathbf{U}_{i,j}^{(0)} = \mathbf{U}_{i,j}^n$ .
2. For  $m = 1, \dots, k + 1$ , compute,

$$\mathbf{U}_{i,j}^{(m)} = \sum_{l=0}^{m-1} \alpha_{ml} \mathbf{U}_{i,j}^{(l)} + \beta_{ml} \Delta t^n (\mathcal{L}_{i,j}(\mathbf{U}^{(l)}) + \mathbf{S}_{i,j}(\mathbf{U}^{(l)})).$$

3. Set  $\mathbf{U}_{i,j}^{n+1} = \mathbf{U}_{i,j}^{(k+1)}$ .

The coefficients  $\alpha_{ml}$  and  $\beta_{ml}$  are given in Table 1.

order	$\alpha_{il}$			$\beta_{il}$		
2	1			1		
	1/2	1/2		0	1/2	
3	1			1		
	3/4	1/4		0	1/4	
	1/3	0	2/3	0	0	2/3

Table 1: Parameters for Runge-Kutta time marching schemes.

#### 4. IMEX-Runge-Kutta methods

IMEX-RK schemes for the balance laws (1.3) are considered by Pareschi and Russo in [9, 10]. Following framework prescribed in [9, 10], an IMEX-RK scheme for (1.3) based on the implicit discretization of the stiff source terms and the explicit discretization of the convective flux when applied to the semi-discrete scheme (3.1), takes the form:

$$\mathbf{U}^{(l)} = \mathbf{U}^n + \Delta t \sum_{m=1}^{l-1} \tilde{a}_{lm} \mathcal{L}(\mathbf{U}^{(m)}) + \Delta t \sum_{m=1}^N a_{lm} \mathbf{S}(\mathbf{U}^{(m)}) \quad (4.1a)$$

$$\mathbf{U}^{n+1} = \mathbf{U}^n + \Delta t \sum_{l=1}^N \tilde{w}_l \mathcal{L}(\mathbf{U}^{(l)}) + \Delta t \sum_{m=1}^N w_l \mathbf{S}(\mathbf{U}^{(l)}). \quad (4.1b)$$

Here, we have ignored the spatial indices  $i, j$  for the sake of notational simplicity. The  $N \times N$  matrices  $\tilde{A} = (\tilde{a}_{lm})$ ,  $\tilde{a}_{lm} = 0$  for  $m \geq l$  and  $A = (a_{lm})$ , are such that the scheme (4.1) is explicit in  $\mathcal{L}$  and implicit in  $\mathbf{S}$ . The IMEX scheme (4.1) can also be characterized with double tableau in the usual Butcher notation:

$$\begin{array}{c|c} \tilde{c} & \tilde{A} \\ \hline & \tilde{w}^\top \end{array} \quad \begin{array}{c|c} c & A \\ \hline & w^\top \end{array}$$

We further assume, that  $a_{lm} = 0$  for  $m > l$  i.e. we consider diagonally implicit Runge-Kutta (DIRK) methods for the source terms. Note it is a sufficient condition to guarantee that  $\mathcal{L}$  is always evaluated explicitly. It has been shown in [9] that scheme (4.1) is asymptotic preserving in the zero relaxation limit for the hyperbolic systems with relaxation. We would like to point out that two-fluid eqns. (1.1) also have stiff source term when  $\hat{r}_g \rightarrow 0$ . However, source term of these equations are oscillatory, in contrast to the diffusive source terms for the hyperbolic systems with relaxation.

In this article, we will consider the two IMEX scheme presented in [9, 10], corresponding to the butcher table 2, and 3.

0	0	0	0	1/4	1/4	0	0
1/2	1/2	0	0	1/4	0	1/4	0
0	1/2	1/2	0	1	1/3	1/3	1/3
	1/3	1/3	1/3		1/3	1/3	1/3

Table 2: IMEX-SSP2(3,3,2) stiffly accurate

0	0	0	0	$\gamma$	$\gamma$	0	0	$\gamma = 1 - \frac{1}{\sqrt{2}}$
1	1	0	0	$1 - \gamma$	$1 - 2\gamma$	$\gamma$	0	
1/2	1/4	1/4	0	1/2	1/2 - $\gamma$	0	$\gamma$	
	1/6	1/6	2/3		1/6	1/6	2/3	

Table 3: IMEX-SSP3(3,3,2) L-stable

s	Number of implicit stages
$\sigma$	Number of explicit stages
p	Overall order of accuracy

Table 4: IMEX scheme notation

In both of these schemes, the explicit part of the table corresponds to SSP $k$  methods, where  $k$  corresponds to the order of explicit part. Implicit part of these schemes is L-stable. Following [9], we denote each scheme with SSP $k(s, \sigma, p)$  where  $s, \sigma$  and  $p$  are expressed in Table 4.

Using the IMEX-FVM (4.1) schemes the numerical solution is updated as follows:

- For  $l = 1, \dots, N$ , Evaluate the following intermediate states,
  1. Explicit convective flux update,

$$\mathbf{U}_*^{(l)} = \mathbf{U}^n + \Delta t \sum_{m=1}^{l-2} \tilde{a}_{lm} \mathcal{L}(\mathbf{U}^{(m)}) + \Delta t \tilde{a}_{ll-1} \mathcal{L}(\mathbf{U}^{(l-1)}). \quad (4.2)$$

2. Implicit stiff source update: Solve

$$\mathbf{U}^{(l)} = \mathbf{U}_*^{(l)} + \Delta t \sum_{m=1}^{l-1} a_{lm} \mathbf{S}(\mathbf{U}^{(m)}) + \Delta t a_{ll} \mathbf{S}(\mathbf{U}^{(l)}), \quad (4.3)$$

for  $\mathbf{U}^{(l)}$ .

- Finally update the solution at the next time level using,

$$\mathbf{U}^{n+1} = \mathbf{U}^n + \Delta t \sum_{l=1}^N \tilde{w}_l \mathcal{L}(\mathbf{U}^{(l)}) + \Delta t \sum_{l=1}^N w_l \mathbf{S}(\mathbf{U}^{(l)}). \quad (4.4)$$

Observe that each intermediate step in the above algorithm requires us to solve (4.3). Usually, this is achieved using an iterative solver (see [2]). However, this can be expensive or may need several iterations to achieve required accuracy. In contrast to [2], we note that the source term of the two-fluid equations (1.1) can split carefully to solve (4.3), exactly. We proceed as follows:

Denote conservative variable  $\mathbf{U} = \{\mathbf{V}_1, \mathbf{V}_2, \mathbf{V}_3\}^\top$  where,

$$\begin{aligned} \mathbf{V}_1 &= \{\rho_i, \rho_e, B^x, B^y, B^z, \psi\}^\top, \\ \mathbf{V}_2 &= \{\rho_i v_i^x, \rho_i v_i^y, \rho_i v_i^z, \rho_e v_e^x, \rho_e v_e^y, \rho_e v_e^z, E^x, E^y, E^z\}^\top, \\ \mathbf{V}_3 &= \{\mathcal{E}_i, \mathcal{E}_e, \phi\}^\top. \end{aligned}$$

We observe that (4.3) can be rewritten in the following 3 blocks,

$$\mathbf{V}_1^{(l)} = \mathbf{G}_1(\mathbf{U}_*^{(l)}), \quad (4.5a)$$

$$\mathbf{V}_2^{(l)} = \mathbf{G}_2(\mathbf{U}^{(1)}, \dots, \mathbf{U}^{(l-1)}, \mathbf{U}_*^{(l)}) + \mathcal{A}(\mathbf{V}_1^{(l)})\mathbf{V}_2^{(l)}, \quad (4.5b)$$

$$\mathbf{V}_3^{(l)} = \mathbf{G}_3(\mathbf{U}^{(1)}, \dots, \mathbf{U}^{(l-1)}, \mathbf{U}_*^{(l)}) + \mathbf{H}(\mathbf{V}_1^{(l)}, \mathbf{V}_2^{(l)}). \quad (4.5c)$$

Here  $\mathbf{G}_1, \mathbf{G}_2$  and  $\mathbf{G}_3$  are the explicit part of (4.3) for the variables  $\mathbf{V}_1, \mathbf{V}_2$  and  $\mathbf{V}_3$  respectively. The Eqns. (4.5) are then solved in sequential manner:

I) Equation (4.5a) is updated explicitly as it involves the evaluation of terms which depends on the known quantities from previous steps.

II) Note that the matrix  $\mathcal{A}(\mathbf{V}_1^{(l)})$  in Eqn. (4.5b) is,

$$\mathcal{A}(\mathbf{V}_1^{(l)}) = \begin{bmatrix} 0 & \frac{B^{z,(l)}}{\hat{r}_g} & -\frac{B^{y,(l)}}{\hat{r}_g} & 0 & 0 & 0 & \frac{\rho_i^{(l)}}{\hat{r}_g} & 0 & 0 \\ -\frac{B^{z,(l)}}{\hat{r}_g} & 0 & \frac{B^{x,(l)}}{\hat{r}_g} & 0 & 0 & 0 & 0 & \frac{\rho_i^{(l)}}{\hat{r}_g} & 0 \\ \frac{B^{y,(l)}}{\hat{r}_g} & -\frac{B^{x,(l)}}{\hat{r}_g} & 0 & 0 & 0 & 0 & 0 & 0 & \frac{\rho_i^{(l)}}{\hat{r}_g} \\ 0 & 0 & 0 & 0 & \frac{B^{z,(l)}}{\hat{r}_{e,g}} & -\frac{B^{y,(l)}}{\hat{r}_{e,g}} & \frac{\rho_e^{(l)}}{\hat{r}_{e,g}} & 0 & 0 \\ 0 & 0 & 0 & -\frac{B^{z,(l)}}{\hat{r}_{e,g}} & 0 & \frac{B^{x,(l)}}{\hat{r}_{e,g}} & 0 & \frac{\rho_e^{(l)}}{\hat{r}_{e,g}} & 0 \\ 0 & 0 & 0 & \frac{B^{y,(l)}}{\hat{r}_{e,g}} & -\frac{B^{x,(l)}}{\hat{r}_{e,g}} & 0 & 0 & 0 & \frac{\rho_e^{(l)}}{\hat{r}_{e,g}} \\ \frac{-r_i}{K} & 0 & 0 & \frac{-r_e}{K} & 0 & 0 & 0 & 0 & 0 \\ 0 & \frac{-r_i}{K} & 0 & 0 & \frac{-r_e}{K} & 0 & 0 & 0 & 0 \\ 0 & 0 & \frac{-r_i}{K} & 0 & 0 & \frac{-r_e}{K} & 0 & 0 & 0 \end{bmatrix} \quad (4.6)$$

with  $\hat{r}_{e,g} = -\hat{r}_g/\lambda_m$  and  $K = \hat{\lambda}^2 \hat{r}_g$ . All the entries in the matrix are already computed in step I. So, we can rewrite Eqn. (4.5b) as,

$$\mathbf{V}_2^{(l)} = \left( \mathbf{I} - (\Delta t)\mathcal{A}(\mathbf{V}_1^{(l)}) \right)^{(-1)} (\mathbf{G}_2(\mathbf{U}^{(1)}, \dots, \mathbf{U}^{(l-1)}, \mathbf{U}_*^{(l)})). \quad (4.7)$$

The term  $\left( \mathbf{I} - (\Delta t)\mathcal{A}(\mathbf{V}_1^{(l)}) \right)^{(-1)} (\mathbf{G}_2(\mathbf{U}^{(1)}, \dots, \mathbf{U}^{(l-1)}, \mathbf{U}_*^{(l)}))$  is evaluated symbolically.

III) The Eqn. (4.5c) is now updated for  $\mathbf{V}_3^{n+1}$  by evaluating  $\mathbf{H}(\mathbf{V}_1^{(l)}, \mathbf{V}_2^{(l)})$ .

In addition to the above scheme we will also consider two more IMEX schemes, namely second order IMEX-SSP2 and third order IMEX-SSP3. These schemes are based on SSP explicit schemes described in Section 3. To obtain these IMEX schemes, each intermediate Euler time update is performed by solving,

$$\mathbf{U}^{(m)} = \Delta t(\mathcal{L}(\mathbf{U}^{(m-1)})) + \Delta t\mathbf{S}(\mathbf{U}^{(m)}) \quad (4.8)$$

for  $\mathbf{U}^{(m)}$ . The eqn. (4.8) can be solved exactly, similar to the Eqn. (4.3). We refer to [11] for more details.

## 5. Numerical Results

In this section, we consider several benchmark test cases for illustrating the efficiency of the IMEX schemes. For the sake of comparison we will also present results for SSP-RK explicit schemes, namely second-order (O2-exp) and third-order (O3-exp) SSP-RK.

### 5.1. Convergence Rates

To compute order of convergence, we construct a smooth solution of (1.1) using *modified* equation:

$$\partial_t \mathbf{u} + \partial_x \mathbf{f}(\mathbf{u}) = \mathbf{s}(\mathbf{u}) + K(x, t).$$

The initial densities are taken to be  $\rho_i = \rho_e = 2.0 + \sin(2\pi x)$ , with the velocities  $v_i^x = v_e^x = 1.0$  and the pressures  $p_i = p_e = 1.0$ . The initial magnetic field is  $B^y = \sin(2\pi x)$  and the initial electric field is  $E^z = -\sin(2\pi x)$ . The computational domain is taken to be  $(0, 1)$  with periodic boundary conditions. To ensure non-vanishing source term we take ion-electron mass ratio to be 2.0. All other physical parameters are assumed to be equal to 1.0. To ensure that the exact solution is

$$\rho_i = 2.0 + \sin(2\pi(x - t)),$$

we take,

$$K(x, t) = \{\mathbf{0}_{13}, -(2 + \sin(2\pi(x - t))), 0, 0, 2 + \sin(2\pi(x - t)), 0\}^T.$$

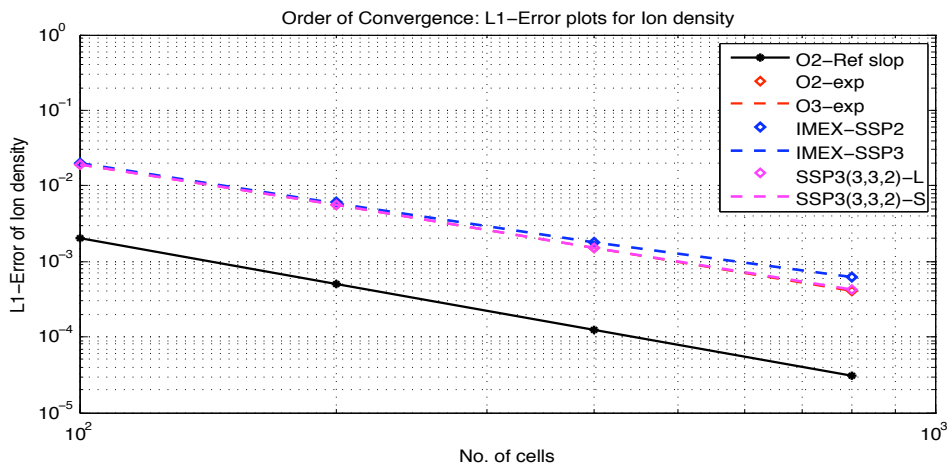


Figure 1:  $L^1$  order of convergence:  $L^1$ -errors of the ion-density at time  $t = 2.0$  are plotted for 100, 200, 400, and 800 cells.

In Figure 1, we have plotted the convergence rates for the different time-stepping schemes based on the second order FVM spatial discretization. We observe that the explicit (O2-exp and O3-exp), SSP3(3,3,2) L-stable (SSP3(3,3,2)-L) and SSP3(3,3,2) stiffly accurate (SSP3(3,3,2)-S) schemes converge with second order. However rate of convergence for the IMEX-SSP2 and IMEX-SSP3 schemes falls as we refine the mesh. This is due to the splitting errors of these schemes.

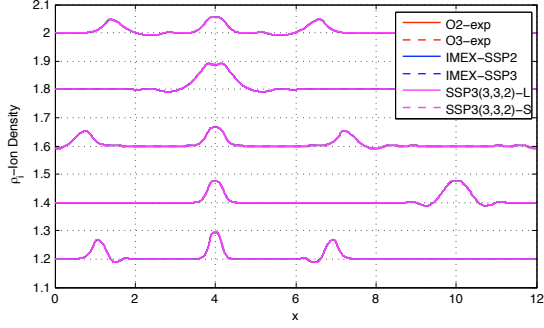
### 5.2. Soliton propagation in one dimension: Low mass ratio

Simulations of soliton formations and interactions in two-fluid plasma are carried out in [1, 5, 6]. We perform two simulations with Larmor radii of 0.01 and 0.0001. The simulation with Larmor radius 0.01 corresponds to the simulations carried out in [1, 5]. Note that low Larmor radius corresponds to the large length scale and (or) large ion charge to mass ratios).

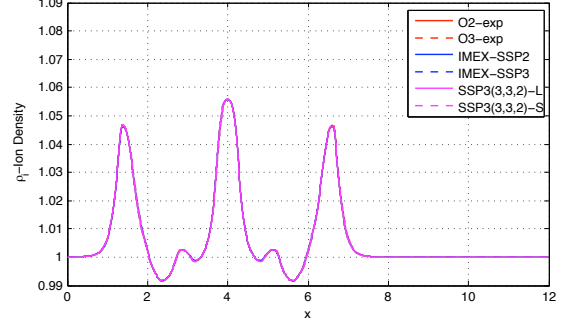
Initially, we assume that plasma is stationary and ion density is given by the smooth *hump*,

$$\rho_i = (1.0 + \exp(-25.0|x - L/3.0|)), \quad (5.1)$$

on domain  $D = (0, L)$  with  $L = 12.0$ . The initial electron pressure is assumed to be  $p_e = 5.0\rho_i$  with initial ion-electron pressure ratio of 0.01. The normalized Debye length assumed to be 1.0, with ion-electron mass ratio of 25. We use periodic boundary conditions to facilitate soliton interaction. The simulations are carried out with 1000 cells.

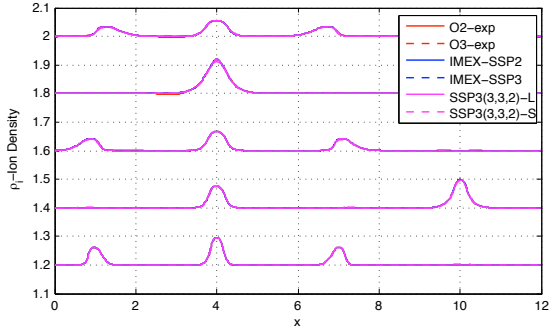


(a) Ion-density at non-dimensional  $t = 1, 2, 3, 4,$  and  $5$

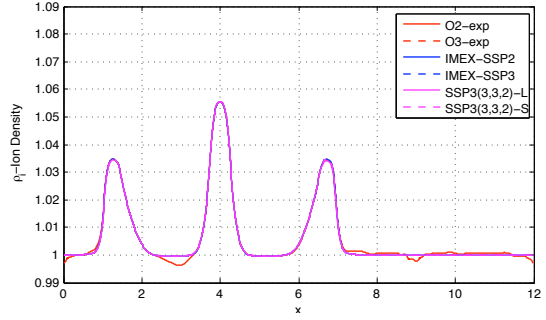


(b) Ion-density comparison of various schemes at non-dimensional time  $t = 5.0$

Figure 2: Soliton propagation in one dimension with 1000 cells and Larmor radius  $\hat{r}_g = 0.01$



(a) Ion-density at non-dimensional  $t = 1, 2, 3, 4,$  and  $5$



(b) Ion-density comparison of various schemes at non-dimensional time  $t = 5.0$

Figure 3: Soliton propagation in one dimension with 1000 cells and Larmor radius  $\hat{r}_g = 0.0001$

Scheme	$\hat{r}_g = 0.01$	$\hat{r}_g = 0.0001$
O2-exp	7.73	1652.68
O3-exp	11.76	144.19
IMEX-SSP2	8.46	8.39
IMEX-SSP3	12.75	12.68
SSP3(3,3,2)-L	13.91	14.74
SSP3(3,3,2)-S	13.74	14.17

Table 5: Comparison of simulation times for soliton propagation in one dimension till  $t = 5.0$  on 1000 cells.

Numerical results are presented in Figure 2 and 4 for the second order schemes with explicit and IMEX time-stepping, and for the Larmor radii of 0.01 and 0.0001. In Figure 2(a) we have plotted the solution at time  $t = 1, 2, 3, 4$  and 5 for the Larmor radius of 0.01. We note that all the schemes are able to capture the soliton waves and produce similar results. In Figure 2(b) we have compared the solutions corresponding to the scheme at non-dimensional time  $t = 5$ . We observe that all the schemes produce comparable results. In Figure 4(a) we have plotted the solution at time  $t = 1, 2, 3, 4$  and 5 for the Larmor radius of 0.0001. Again we note that soliton waves are captured by all the schemes. From the solution plots at non-dimensional time  $t = 5$  in Figure 4(b), we observe that O2-exp produce some oscillations. These oscillations do disappear if we use smaller time steps. All other schemes produce comparable results.

In Table 5, we have presented the simulation times of different time-stepping methods in seconds on the four computational cores for Larmor radii of 0.01 and 0.0001. In the case of  $\hat{r}_g = 0.01$ , the time step is dictated by CFL condition due to fastest wave speed. We note that, simulation times of two step methods O2-exp and IMEX-SSP2 are comparable, with O2-exp being slightly faster. Similarly, simulation times of the three step methods, O3-exp, IMEX-SSP3, SPP3(3,3,2)-L and SSP3(3,3,2)-S are comparable, with O3-exp being the fastest. This is due to the evaluation of the matrix inverse for the source update in IMEX schemes. We also note that IMEX-SSP3 is slightly faster than SSP3(3,3,2)-L and SSP3(3,3,2)-S scheme. Furthermore, three step methods are approximately 50 percent more expansive than the two step methods, due to computation of an additional intermediate step. In the case of  $\hat{r}_g = 0.0001$  the time step is dictated by the stiffness of the source. In this case we note that simulation time of O2-exp has increase by two orders of magnitude. Third order explicit scheme O3-exp perform better, still simulation time needed is almost 12 times than that of non-stiff case with  $\hat{r}_g = 0.01$ . For the IMEX schemes we note that simulations times are similar to the case of  $\hat{r}_g = 0.01$ .

### 5.3. Soliton propagation in one dimension: Realistic mass ratio

In this section, we will simulate soliton propagation in one-dimension with realistic mass ratio  $m_i/m_e = 1836$  and Larmor radius of  $\hat{r}_g = 0.0001$ . The initial ion-density is,

$$\rho_i = (1.0 + M \exp(-25.0|x - L/3.0|)) \quad (5.2)$$

with  $M = 2.0$  on the computational domain  $(0, L_x)$  with  $L_x = 12.0$ . All other initial and boundary conditions are the same as in the previous section 5.2.

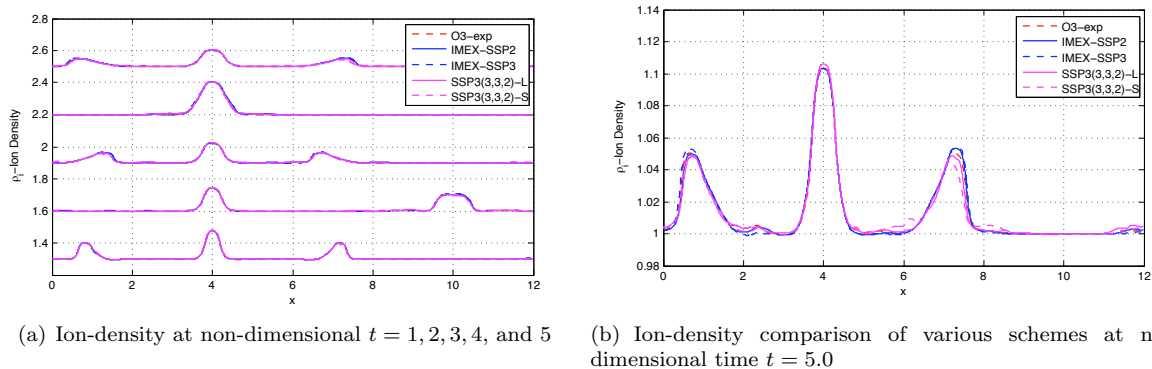


Figure 4: Soliton propagation in one dimension with 2500 cells and Larmor radius  $\hat{r}_g = 0.0001$

Numerical solutions using 2500 cells are presented in Figure 4 . In Figure 4(a), we have plotted the ion density at non-dimensional times  $t = 1, 2, 3, 4$  and 5. We note that all the schemes are able to capture the soliton waves and their interactions. In Figure 4(b), we have plotted the solution at time  $t = 5.0$ . We observe that all the schemes have comparable results. Also, SSP3(3,3,2)-S scheme produce small oscillations, but

Scheme	Simulation time
O3-exp	2287.88
IMEX-SSP2	327.91
IMEX-SSP3	479.97
SSP3(3,3,2)-L	617.23
SSP3(3,3,2)-S	569.14

Table 6: Comparison of simulation times for one dimensional soliton propagation with mass ratio of 1836 and Larmor radius 0.0001

these oscillations are stable and disappear with further mesh refinement. These simulations are performed on 10 computational cores. In Table 6 we have presented the simulation time for the schemes. We note that the simulation time of O3-exp scheme is four times more than the IMEX schemes. The simulation time of the IMEX schemes is comparable. We have ignored O2-exp scheme due to large computation time.

#### 5.4. Generalized shock tube Riemann problem

The initial conditions for the Riemann problem are,

$$\mathbf{U}_{\text{left}} = \begin{cases} \rho_i = 1.0 \\ p_i = 5 \times 10^{-5} \\ \rho_e = 1.0 \ m_e/m_i \\ p_e = 5 \times 10^{-5} \\ B^x = 0.75 \\ B^y = 1.0 \\ \mathbf{v}_i = \mathbf{v}_e = \mathbf{E} = 0 \\ \phi = \psi = B^z = 0 \end{cases} \quad \mathbf{U}_{\text{right}} = \begin{cases} \rho_i = 0.125 \\ p_i = 5 \times 10^{-6} \\ \rho_e = 0.125 \ m_e/m_i \\ p_e = 5 \times 10^{-6} \\ B^x = 0.75 \\ B^y = -1.0 \\ \mathbf{v}_i = \mathbf{v}_e = \mathbf{E} = 0 \\ \phi = \psi = B^z = 0 \end{cases} \quad (5.3)$$

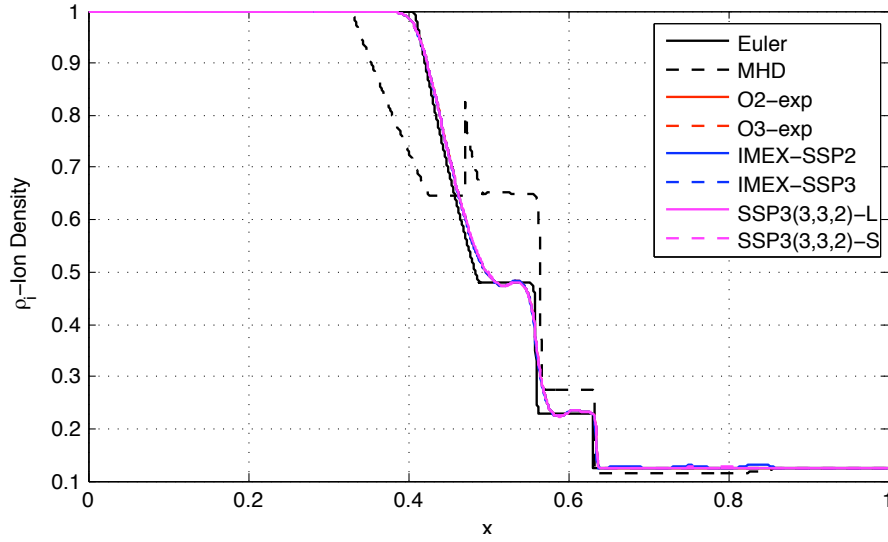
on a domain  $(0, 1)$  with,  $\mathbf{U} = \mathbf{U}_{\text{left}}$  for  $x < 0.5$  and  $\mathbf{U} = \mathbf{U}_{\text{right}}$  for  $x > 0.5$ . The ion-electron mass ratio is taken to be 1836. The problem is nondimensionalized using  $p_0 = 10^{-4}$  which results in the normalized speed of light  $\hat{c} = 100$ . Non-dimensional Debye length is taken to be 0.01. We compute solutions using non-dimensional Larmor radii of 100 and 0.001 and use Neumann boundary conditions.

Numerical solutions are presented in Figure 5. In Figure 5(a) we have plotted the numerical solutions at Larmor radius of  $\hat{r}_g = 100$ . We expect solutions to be close to the corresponding ion Euler gas flow solution. We observe that all the scheme produce solution close to Euler solution. Furthermore all the schemes produce comparable results with 1000 cells. The simulation times for the explicit and implicit schemes are similar in this case.

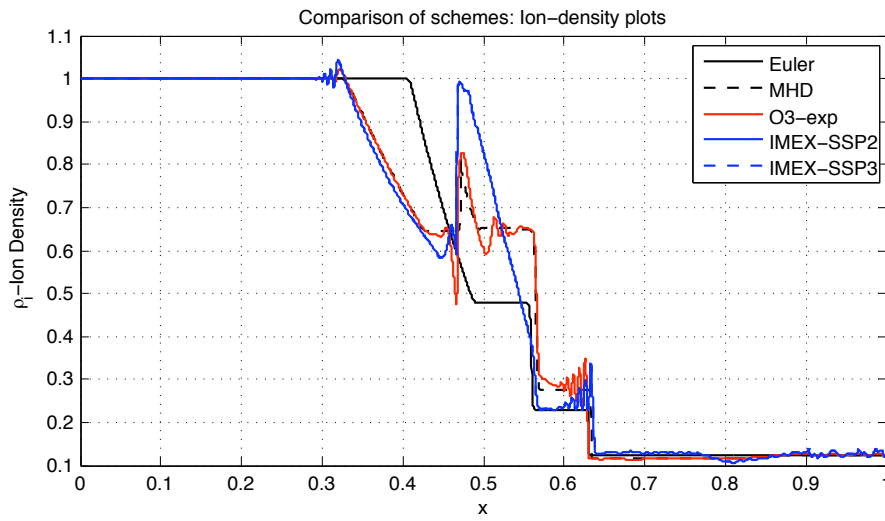
In Figure 5(b) we have plotted solution at 20000 cells corresponding to the Larmor radius of 0.001 for the O3-exp, IMEX-SSP2 and IMEX-SSP3 schemes. We have have ignored other schemes due to significantly large simulation times. We note that solution for all the schemes is converging to the MHD solution with O3-exp solution being the closest. Both IMEX schemes fails to capture contact discontinuity wave. These simulations are carried out on 32 computational cores. The simulation times for O3-exp, IMEX-SSP2 and IMEX-SSP3 scheme are 4506.8, 13905.5 and 20610.4 seconds, respectively. We note that although IMEX scheme are not efficient in this case, stiffness in the source is due to the low Debye length compare to the soliton case where stiffness was primarily due to low Larmor radius.

#### 5.5. Soliton Propagation in two dimensions

Soliton in two fluid plasma in two dimension were simulate in [6]. However non-physical mass ratio and Larmor radius were used in simulations in order to avoid stiff source terms. In this Section we will simulate

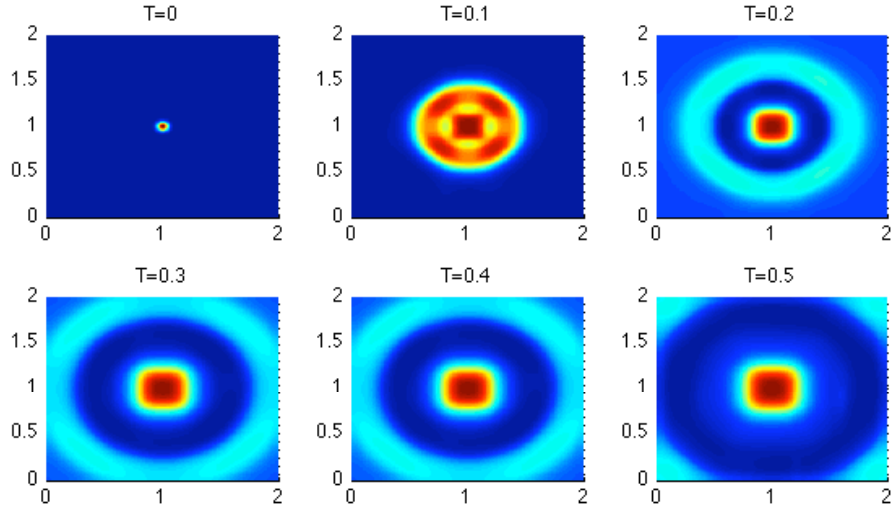


(a) Ion-density plots with Larmor radius  $\hat{r}_g = 100$  and 1000 cells

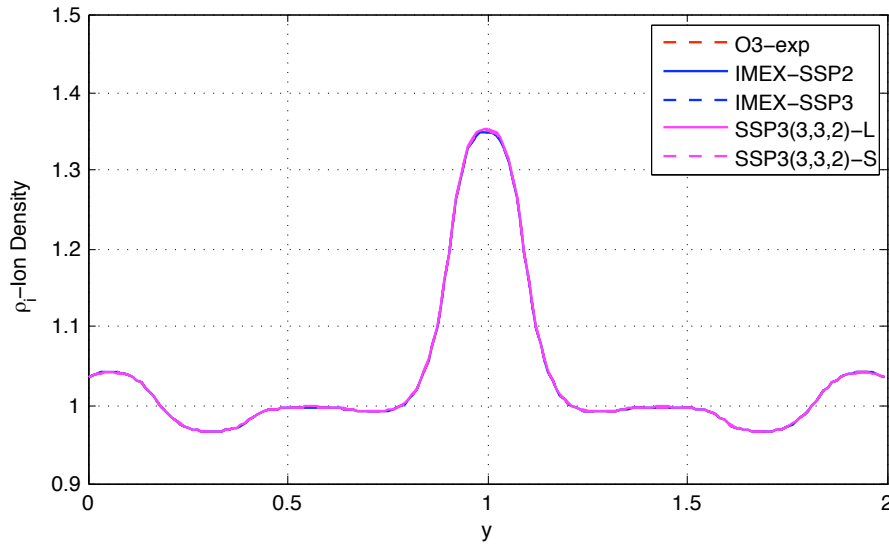


(b) Ion-density plot for Larmor radius  $\hat{r}_g = 0.001$  on 20000 cells

Figure 5: Bri-Wu shock tube problem: Solution at non-dimensional time  $t = 0.1$



(a) Ion-density at non-dimensional  $t = 0, 0.1, 0.2, 0.3, 0.4,$  and  $0.5$  with SSP3(3,3,2)-S scheme.



(b) Ion-density plot of solution along the line  $x = 1$  at non-dimensional time  $t = 0.3$

Figure 6: Soliton propagation in two dimensions with mass ratio of 1836, and Larmor radius  $\hat{r}_g = 0.0001$  using  $200 \times 200$  cells

soliton in two dimensions using realistic mass ratio of 1836 and Larmor radius of 0.0001. We consider initial ion density of,

$$\rho_i = 1.0 + 5.0 \exp(-500.0((x - L_x/2.0)^2 + (y - L_y/2.0)^2)) \quad (5.4)$$

on the computational domain  $(0, L_x) \times (0, L_y)$  with  $L_x = L_y = 2.0$ . All other initial conditions and physical parameters are same as in the case of one dimensional soliton propagation in Section 5.2. We use Neumann boundary conditions.

Numerical simulations are carried out using  $200 \times 200$  cells on 10 computational cores. The results are presented in Figure 6. In Figure 6(a), we have plotted the solution at non-dimensional time of  $t = 0, 0.1, 0.2, 0.3, 0.4$  and  $0.5$  using SPP3(3,3,2)-S time stepping routine. We note that initial density hump breakdown, which results in to a radial wave moving outward. The wave structure is similar to the one dimensional case (see 5.3). In Figure 6(b) we have plotted ion-density along the line  $x = 1.0$  for the scheme at time  $t = 0.3$ . We observe that all the schemes produce comparable results. Simulation time for the

Scheme	<i>Simulationtime</i>
O3-exp	8039.16
IMEX-SSP2	1141.26
IMEX-SSP3	1596.34
SSP3(3,3,2)-L	1926.75
SSP3(3,3,2)-S	1924.84

Table 7: Comparison of simulation times for two dimensional soliton simulation.

schemes are presented in Table 7. Similar to the one dimensional case (see 5.3), we see that O3-exp scheme is about four time computationally expensive than the IMEX schemes. Furthermore, in three step IMEX schemes, IMEX-SSP3 is the least expensive.

## 6. Conclusion

We have presented several IMEX-FVM schemes for the two fluid MHD equations based on the explicit evaluation of the numerical flux and implicit treatment of the source terms. These schemes are then benchmarked and compared using several numerical examples. The IMEX scheme are shown to be computationally efficient for the low Larmor radius.

## Acknowledgement

Author would like to thank Prof. Siddhartha Mishra (SAM, ETH Zurich) for his valuable comments.

## References

- [1] A. HAKIM, J. LOVERICH AND U. SHUMLAK. *A high-resolution wave-propagation scheme for ideal two-fluid plasma equations*. J. Comp. phys. 219 (2006), 418-442.
- [2] U. SHUMLAK AND J. LOVERICH. *Approximate Riemann solvers for the two-fluid plasma model*. J. Comp. Phys. 187 (2003), 620-638.
- [3] C. D. MUNZ, P. OMNES, R. SCHNEIDER, E. SONNENDRU KER, U. VO $\beta$  *Divergence correction techniques for Maxwell solvers based on a hyperbolic model*, J. Comp. Phys. 161 (2000), 484-511.
- [4] R.J. LEVEQUE *Finite Volume Methods For Hyperbolic Problems* Cambridge University Press, Cambridge, 2002
- [5] BABOOLAL, S., BHARUTHRAM, R., *Two-scale numerical solution of the electromagnetic two-uid plasma-Maxwell equations: Shock and soliton simulation*, Math. and Comp. in Simulation, Vol. 76 (2007), pages 3-7.
- [6] BABOOLAL, S., *High-resolution numerical simulation of 2D nonlinear wave structures in electromagnetic fluids with absorbing boundary conditions*, J. Comp. Appl. Math., Vol. 234 (2010), pages 1710-1716.
- [7] J. BALBAS, E. TADMOR, C.C. WU *Non-Oscillatory central schemes for one- and two-dimensional equations I*, J. Comput. Phys. 201(2004)261285.

- [8] S. GOTTLIEB, C. W. SHU, E. TADMOR, *Strong stability-preserving high-order time discretization methods*, SIAM Rev., 43 (2001), 89-112.
- [9] PARESCHI L., RUSSO G., *Implicit-Explicit Runge-Kutta methods and applications to hyperbolic systems with relaxation*, J. Sci. Comput. 25 (2005), no. 1-2, 129–155.
- [10] PARESCHI L., RUSSO G., *On the stability of Implicit-Explicit Runge-Kutta schemes for systems of balance laws*, (2007)
- [11] H. KUMAR, MISHRA S., *Entropy stable numerical schemes for two-fluid MHD equations*, Submitted.

# Research Reports

No.	Authors/Title
11-26	<i>H. Kumar</i> Implicit-explicit Runge-Kutta methods for the two-fluid MHD equations
11-25	<i>H. Papasaïka, E. Kokiopoulou, E. Baltasvias, K. Schindler and D. Kressner</i> Sparsity-seeking fusion of digital elevation models
11-24	<i>H. Harbrecht and J. Li</i> A fast deterministic method for stochastic elliptic interface problems based on low-rank approximation
11-23	<i>P. Corti and S. Mishra</i> Stable finite difference schemes for the magnetic induction equation with Hall effect
11-22	<i>H. Kumar and S. Mishra</i> Entropy stable numerical schemes for two-fluid MHD equations
11-21	<i>H. Heumann, R. Hiptmair, K. Li and J. Xu</i> Semi-Lagrangian methods for advection of differential forms
11-20	<i>A. Moiola</i> Plane wave approximation in linear elasticity
11-19	<i>C.J. Gittelsohn</i> Uniformly convergent adaptive methods for parametric operator equations
11-18	<i>E. Kokiopoulou, D. Kressner, M. Zervos and N. Paragios</i> Optimal similarity registration of volumetric images
11-17	<i>D. Marazzina, O. Reichmann and Ch. Schwab</i> <i>hp</i> -DGFEM for Kolmogorov-Fokker-Planck equations of multivariate Lévy processes
11-16	<i>Ch. Schwab and A.M. Stuart</i> Sparse deterministic approximation of Bayesian inverse problems
11-15	<i>A. Barth and A. Lang</i> Almost sure convergence of a Galerkin–Milstein approximation for stochastic partial differential equations
11-14	<i>X. Claeys</i> A single trace integral formulation of the second kind for acoustic scattering